Integrated Computational Alloy Design of Nickel-Base Superalloys

M. MONTAKHAB and E. BALIKCI

The nickel-base superalloys are unsurpassed for hot sections of the gas turbine engines whose efficiency can be improved by developing new superalloys with enhanced properties. The artificial neural networks (ANN) method is utilized in alloy design of single-crystal nickel-base superalloys. The ANN method is especially powerful in applications where developing a physically sound model is challenging such as alloy design with multiple components. A design space of 45,000 alloy compositions is generated, and then a multilayer perceptron (MLP) feed-forward (FF) artificial neural network is used to predict the density and creep lives of these alloys. The ANN method is coupled with physics-based (PHACOMP) calculations to predict and then correlate the creep rupture life to the composition, precipitate volume fraction, topologically closed packed phases, temperature, and stress. Then, an experimental alloy composition is selected from the design space, and its solidification behavior is investigated by a thermodynamics (CALPHAD)-based software. Moreover, single-crystal rods of the experimental alloy are grown and machined into creep samples, which are creep tested at three different stress–temperature couples. A good match between the experimental results and the ANN predictions is displayed in scatter plots and in Larson–Miller plots for the experimental alloy and for selected, well-known commercial single-crystal alloys. As the correlation of the microstructure to mechanical properties is still in its infancy by thermodynamics and mechanics-based software, an integrated ANN modeling is shown to be a powerful tool for finding a composition and establishing relationships between the microstructure and properties of alloys. This, of course, can help reduce the material development cycle time as aimed by the Integrated Computational Material Engineering (ICME).

https://doi.org/10.1007/s11661-019-05252-7

I. INTRODUCTION

CONVERSION efficiency of gas turbine engines increases with an increased turbine entry temperature,[1] which is attainable by availability of materials durable at high temperatures. A good combination of creep resistance, microstructure stability, and corrosion/oxidation resistance provided by Ni-base superalloys, makes them unsurpassed candidates as hot section turbine engine materials. The high-temperature durability of these alloys are achieved by a high-volume fraction of a strengthening gamma-prime (γ') precipitate phase with an ordered face-centered cubic crystal structure embedded in a disordered face-centered cubic gamma (γ) matrix.[1–3] Lightweight silicide-, nitride-, and aluminide-based ceramics and intermetallics are aimed to substitute for superalloys in turbine engines due to their lower density and higher temperature capability. However, their application is limited by their brittle nature.[4] Therefore, designing superalloys with increased temperature capability, improved life, and reduced density is of a crucial importance in aerospace and power industries.

A significant improvement has been achieved over the many years in the high-temperature performance of Ni-base superalloys despite an Edisonian alloy development approach that relies on extensive experimentation in various stages of the alloy development from a concept to a validated part.[5] More than 10 alloying elements are present in superalloys, which makes the traditional experimental alloy design methods very time consuming and costly. As a result, the alloy development cycle is far behind the product development cycle. The materials community has decided to overcome this *via* the Materials Genome Initiative (MGI) and Integrated Computational Materials Engineering (ICME).[6] Computational methods reduce the materials development cycle to keep pace with very fast developing product design and development and hence enable

M. MONTAKHAB and E. BALIKCI are with the Department of Mechanical Engineering, Bogazici University, 34342 Istanbul, Turkey. Contact e-mail: ercan.balikci@boun.edu.tr
Manuscript submitted December 31, 2018.
Article published online May 13, 2019

development of new alloys to meet cost/performance requirements.[7] These methods should consider several parameters that are interlinked in a complex way. A partial list of these parameters can include the size, distribution, and volume fraction of the precipitates, the ordered nature of the precipitates, lattice misfit between the precipitates and the matrix, temperature, stress, and environmental conditions. Recently, a number of software are developed to model thermodynamics, diffusion, microstructure, and mechanical properties.[8–10] The existing software for mechanical properties is based on simplified empirical approaches, and so they are unable to make a full correlation between influencing parameters.[11,12] Mechanical properties depend not only on the atomic bonding and the atomic/molecular arrangement, but they are also strongly influenced by the morphology, distribution, and amount of multiple phases, and interface strength, which are all determined by the chemical composition of the alloy at given operating conditions. In fact, interdependence of all these makes it a challenging task to develop a unique, physically sound model to predict the long-term properties of superalloys.

A major deformation mode in the hot sections of turbine engines is the creep. While optimizing the chemistry of an alloy to attain a high creep resistance, a particular attention should be given to lowering the density of the alloy. Suggested methods for density estimation suffer either from low accuracy due to complex interatomic bonding, or they do not include all candidate alloying elements generally used in superalloys.[11,13] Addition of heavy refractory elements in later generations of single-crystal superalloys to reduce the diffusion and hence to increase the creep life has led to an increase in the density, which adversely affects the energy efficiency of the turbine engines.[14] In addition, formation of the harmful TCP (topologically close packed) phases such as Mu, P, Sigma, and Laves[15] puts a limit on the amount of the refractory alloying additions. The d-electrons concept based on the PHACOMP (PHAse COMPutation) method gives a good measure of the susceptibility for the TCP phase formation and the gamma-prime (γ') precipitate phase volume fraction,[16–18] which can also be determined by a very few thermodynamics-based commercial software.[8–10]

As the modeling of interdependence of composition, microstructure, properties, and performance in alloys is a challenging task by physics and thermodynamics-based models, the artificial neural network (ANN) method appears to be a powerful approach for alloy design. The artificial neural network has been effectively used in alloy design and modeling the mechanical, thermal, and physical properties of a variety of different alloy systems such as carbon steels,[19–23] austenitic stainless steels,[24] titanium alloys,[25] aluminum,[26,27] molybdenum,[28] and polycrystal and single-crystal Ni-based superalloys.[29,30] It has also been successfully used for modeling the process parameters in a number of manufacturing processes.[31–33] Moreover, ANN has found applications in image analysis for classification of defects in cast parts and in crept microstructures.[34,35] Successful application of ANN particularly for design of Ni-based superalloys has been reported in the literature for predicting the thermal expansion,[36] yield and tensile strength,[37–39] creep and fatigue life,[38–40] and lattice parameters of the matrix and precipitate.[41]

This current study utilizes the artificial neural network (ANN) modeling, integrated with the physics-based PHACOMP and thermodynamics-based CALPHAD (CALculation of PHAse Diagrams), for the alloy design of Ni-base superalloys. Thus, the current work differs from other studies in the literature by an integrated alloy design approach that uses beneficial aspects of the artificial neural networks, PHACOMP, and CALPHAD. The artificial neural networks use known examples (input) to infer rules for estimating correct output that essentially unveils concealed patterns in the input data. It is here shown that this method is capable of correlating the chemistry of the alloys and their operating conditions to the creep rupture life. The model also provides very accurate density predictions. The γ' volume fraction and the propensity for TCP formation are calculated by the PHACOMP method.[16–18] The γ' volume fraction is used as one of the inputs to the network, but the TCP formation, judged by the M_d number, is used in post-processing of the ANN data. The effect of alloying elements on the volume fraction of the γ' and formation of the TCP phases and then their effect on the creep resistance are investigated, and combined effects are illustrated in scatter plots. In addition, single-crystal samples of an experimental alloy with the third-generation composition are grown. The composition of this alloy is within the design space whose properties are predicted by the current ANN. Following an aging treatment, creep experiments of this alloy are conducted and the results are compared to the ANN predictions. The promising results achieved in this study can aid alloy designers/manufacturers to reduce the degree of empiricism inherent in many previous treatments and reduce the number of trial experiments when developing new alloys.

II. ARTIFICIAL NEURAL NETWORK MODEL AND EXPERIMENTAL VERIFICATION

Artificial neural network models are exceptionally useful in complex pattern recognition and function approximation tasks where other techniques are not able to notice the trend. Therefore, they are especially used in places where there is not a physically sound model such as alloy design with multiple components. Among various types of artificial neural networks, the multilayer perceptron (MLP) feed-forward network is a commonly used one due to relative ease in implementation and lower number of required training samples.[42] Hence, an MLP developed in Matlab is used in the present study. The architecture of the MLP used in the current study is schematically shown in Figure 1, which includes an input layer (X_i), a processing unit called hidden layer (a_j), and an output layer (O). The hyperbolic tangent and linear transfer functions[42,43] are used, respectively, in the hidden and output layers. The weights $W_{i,j}$ are

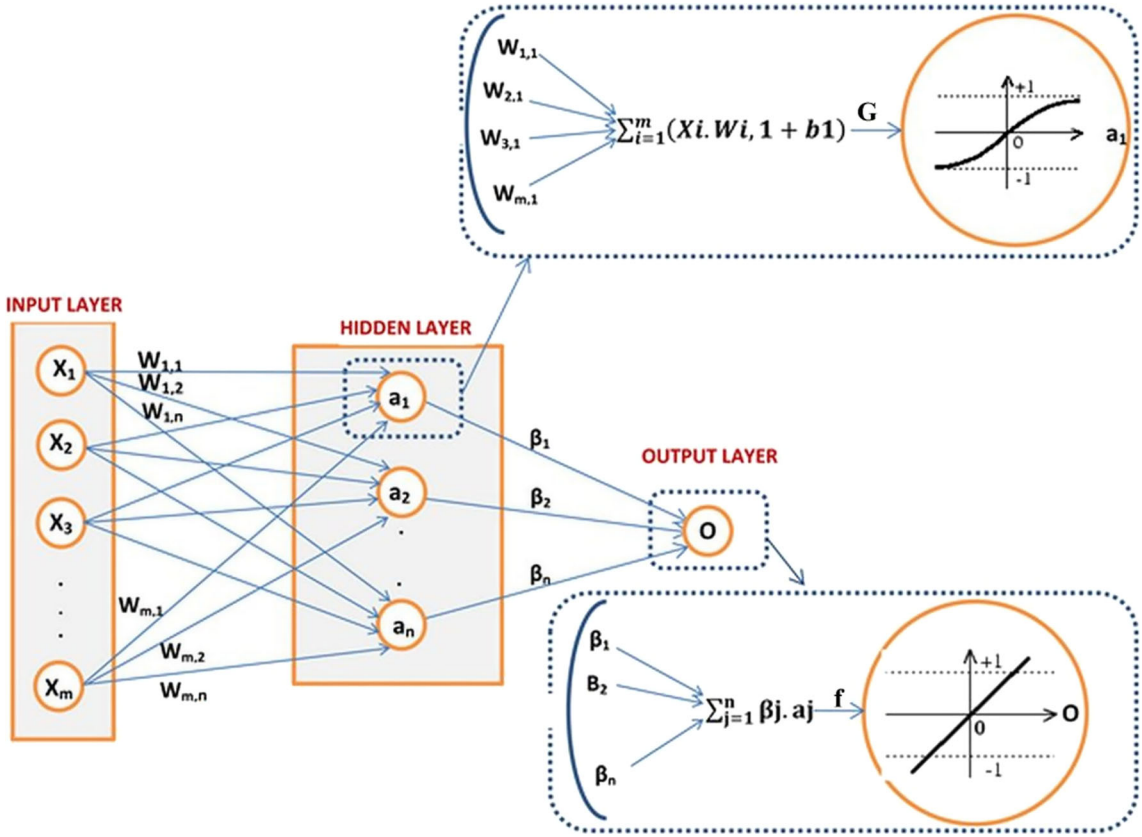

Fig. 1—Schematic architecture of the MLP used in this study showing the input, hidden, and output layers.

assigned for the connections between the input and the hidden layers and β_j are between the hidden and output layers. The Bayesian Regularization (BR) backpropagation algorithm[44,45] is used to adjust the weights in neurons after each iteration in order to increase the accuracy in the output.

A Ni-base superalloy database for the training and testing of the artificial neural network model is formed by collecting data from the open literature, comprised of articles and patents. The database contains 260 single-crystal superalloys for the density modeling and 1250 datasets for the creep rupture time. The test temperature ranges from 750 °C to 1200 °C and the test stress ranges from 30 to 845 MPa in the alloy database for the rupture time which itself ranges from 15 to 1050 hours. Eighty percent of the literature data is selected randomly to train the network and the remaining twenty percent is used to test the performance of the trained network.

MLP architectures of 10-8-1 and 14-10-1 are developed for modeling the density and rupture time, respectively. The network has 10 input nodes (concentration of 10 alloying elements) for the density modeling and 14 input nodes (concentration of 10 alloying elements, volume fraction of the γ' phase, density, temperature, and stress) for the rupture time modeling. The number of neurons (nodes) for the hidden layer (8 for the density and 10 for the rupture time) is selected based on the error level of the network. Both networks have one output node, which is the density or rupture time. The error of the network is determined for the training and testing of the network for both the density and rupture life estimation as presented in Figures 2(a) and (b). It is seen that by increasing the number of nodes in the hidden layer, the network error decreases. Beyond 8 nodes in the density modeling and 10 nodes in the rupture time modeling, the error of the network is stable.

An alloy design space is created using randomly generated numbers in the composition ranges for elements shown in Table I. Obviously, an alloy design space can cover infinite number of alloys depending on the composition resolution. For the ANN modeling, forty-five thousand (45,000) alloy compositions are generated. The volume fraction of the γ' phase[16] and the M_d value[18] for each alloy in the generated design space are determined according to the PHACOMP model. The artificial neural network then has predicted the rupture time and density for the generated 45,000 alloy compositions.

An experimental alloy (named ERBALLOY) with the third-generation composition (Table II) and a moderate rupture time is selected from the design space. In fact, ERBALLOY composition differs from the second-generation commercial single-crystal superalloy CMSX-4 composition only by 2 pct more Re, which makes it a third-generation superalloy. Although we have tried, it has been impossible to prepare (melt) alloy

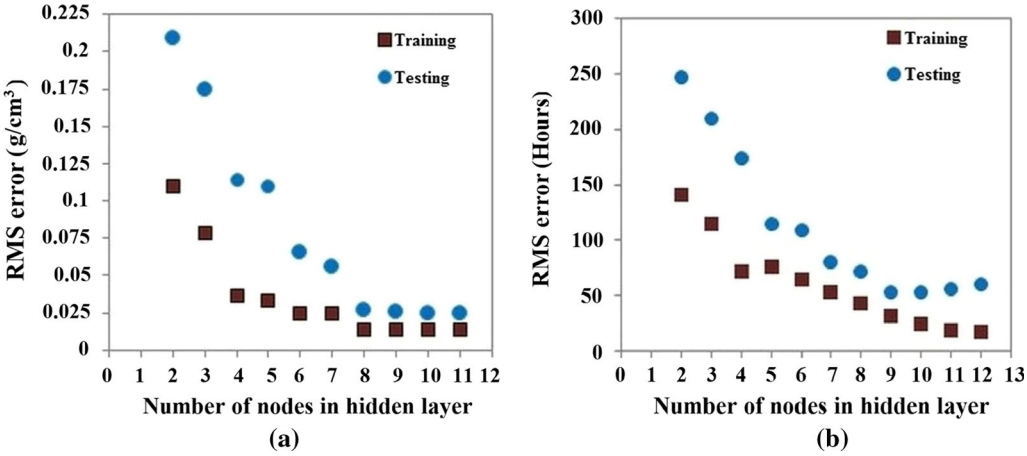

Fig. 2—Error for training and testing the networks with different numbers of hidden nodes for estimation of (*a*) density and (*b*) rupture time.

compositions with much higher rupture time predicted by the integrated ANN approach in this study. Please see Section III for predicted alloy properties by the ANN method. Hence, we have used CMSX-4 as a master alloy to prepare ERBALLOY which is processible in our laboratory. Despite its lower rupture time compared to alloys in its generation, utilization of ERBALLOY for the purpose of delineating the steps and procedures in an alloy development program is crucial and instructive. Solidification range (1403 °C to 1354 °C) and precipitate solvus temperature (1250 °C) of ERBALLOY are determined by Thermo-Calc (CALPHAD) using the TCNI7 database. Then, samples of this alloy are grown in [001] direction as single-crystal rods of 15 mm diameter and 90 mm length by the Vertical Bridgman method.[46] Creep test samples with 6 mm reduced diameters are machined according to the ASTM E139. The samples are then subjected to a step-wise solution treatment to prevent incipient melting according to 1280 °C/2 hours + 1290 °C/2 hours + 1300 °C/2 hours + 1305 °C/2 hours + 1315 °C/4 hours/Water Quench. The solution-treated microstructure contains cuboidal precipitates with a unimodal size distribution and a mean edge size of 90 nm. Following the solution treatment, the samples are first aged at 1140 °C/6 hours/Water Quench and then at 870 °C/24 hours/Water Quench. Thus, creep samples have a bimodal precipitate size distribution containing 48-nm-diameter spheroidal and 327-nm-edge-length cuboidal precipitates. These precipitate sizes are determined by ImageJ software from the digital Scanning Electron Microscope (SEM) images. Similarly, precipitate volume fraction is determined by ImageJ software to be about 70 pct after aforementioned heat treatment. Nevertheless, the volume fraction of the precipitates at room temperature following solidification is predicted by both PHACOMP and CALPHAD (Thermo-Calc) as 58 pct. Then, the creep behavior of this alloy is determined in three different test conditions at 750 °C/750 MPa, 982 °C/248 MPa, and 1100 °C/137 MPa according to ASTM E139.

III. RESULTS AND DISCUSSION

A major objective in the design of superalloys used in the hot sections of the turbine engines is to come up with alloy compositions that provide a high creep life with a low alloy density. Of course, there are other equally important parameters like the oxidation resistance, hot corrosion resistance, castability, and cost which are affected by the chemical composition of the alloy.[2,11] Although the latter properties could also be included in the artificial neural network model, this study focusses only on the former properties to fit the results within publishable number of pages. The density of an alloy is predicted based on the amount and atomic weights of the elements forming the alloy, while the creep rupture life is related to the elements in the alloy, volume fraction of γ', M_d values, stress, and temperature.

The training and testing of the network are accomplished by comparing the predicted values and the experimental (literature) ones. A network with one hidden layer that contains eight neurons is observed to perform with the lowest error (Figures 3(a) and (b)) for the density estimation. Likewise, a network with one hidden layer and ten neurons has the best performance for the rupture time estimation as seen in Figures 3(c) and (d). It is apparent that the artificial neural network model performs very well in modeling the density and rupture time with the correlation levels of 99.3 and 92.7 pct, respectively. Clearly, the prediction accuracy for the rupture time is lower. The rupture time depends on other parameters (*i.e.*, temperature and stress) than the chemistry of the alloy alone, which increases the sensitivity of the experiments and causes fluctuations in the experimental data. Since the input data are gathered from published papers and patents, the unknown inaccuracy of the input data is conveyed to the network.

The density, volume fraction of the γ', and M_d distributions of the alloys in the entire design space are shown in Figure 4. The spread is between 8 and 9.6 g/cm^3 for the density, 40 and 95 pct for the γ' volume fraction, and 0.9 and 1.08 eV for the M_d. The respective peaks occur at 8.6 to 8.7 g/cm^3, 60 to 65 pct,

Table I. Composition Ranges Used to Generate the Alloy Design Space

Element	Ni	Re	Cr	W	Co	M	Hf	Ti	Al	Ta
Range (Wt Pct)	bal.	0 to 6	0 to 10	0 to 10	0 to 10	0.6	0.1	1	3 to 7	0 to 10

Table II. Composition of ERBALLOY

Element	Ni	Re	Cr	W	Co	M	Hf	Ti	Al	Ta
Range (Wt Pct)	bal.	5.0	7.1	6.5	9.3	0.5	0.0	0.8	5.0	5.5

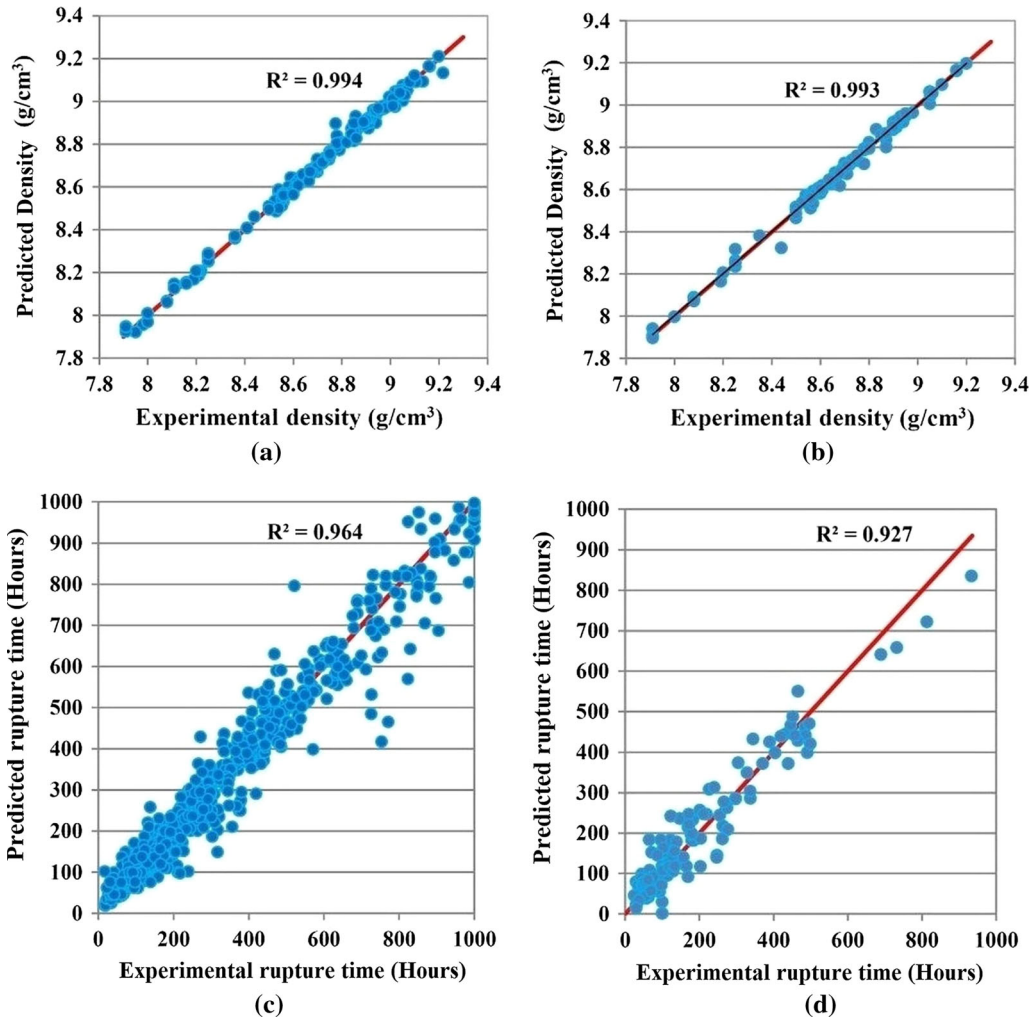

Fig. 3—The ANN-predicted values are plotted against the known values for the density and rupture time after training (*a* density, *c* rupture time) and testing (*b* density, *d* rupture time).

and 0.97 to 0.98 eV. These histograms show symmetric normal distributions, and the peak values match the typical properties of the commonly known single-crystal superalloys, which indicate a well-representing alloy design space.

The average creep rupture lives of the alloys in the design space are determined for various composition ranges of a selected element (Re, Cr, Al, and Ta/W), and the results are plotted in Figure 5. Obviously, these plots can be generated for any element in the alloy composition. The increased Re content substantially increases the rupture life. Re partitions preferentially to the matrix (γ) and is a strong solid solution strengthener of the matrix in the Ni-based single-crystal superalloys.[15] Re is also a slow diffusing element in the matrix which is the main reason for the rhenium effect, increasing the rupture

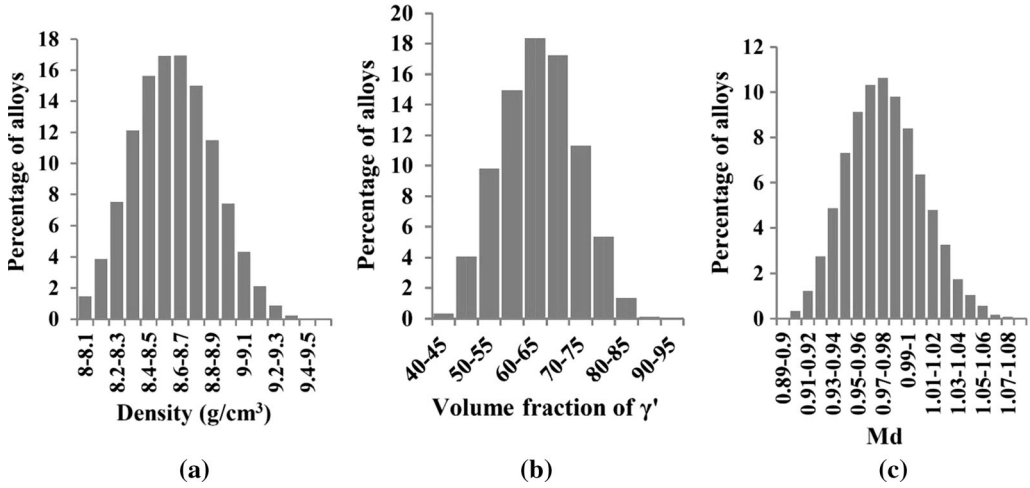

Fig. 4—Percentage of the alloys *vs* density (*a*), volume fraction of γ' (*b*), and M_d (*c*).

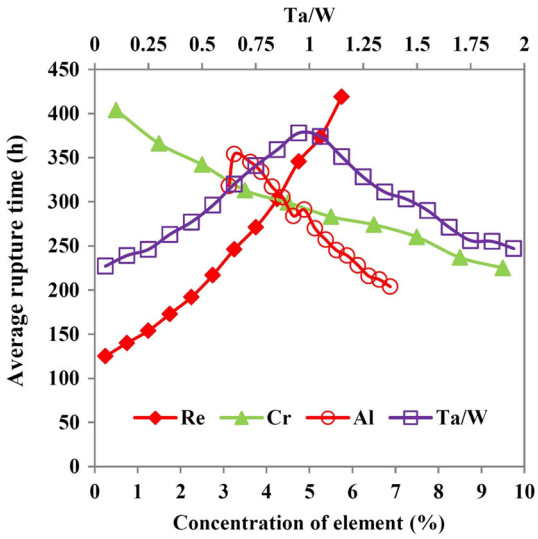

Fig. 5—Rupture time *vs* concentration of Re, Cr, and Al. The secondary top axis shows rupture time *vs* ratio of Ta/W.

strength.[47–49] Unfortunately, like other refractory elements, Re increases the tendency for the TCP phase formation which is predicted in this study by utilizing M_d.[16] A high M_d number increases the propensity. Due to the Re's high M_d number, the overall M_d number of an alloy containing Re increases.[50] Figure 6 plots M_d *vs* the volume fraction of γ'. The first row (Figures 6(a) through (c)) shows the percentage of alloys *vs* M_d for the specified concentration ranges of the elements Re, Cr, and Al. In M_d *vs* volume fraction of the γ' scatter plots, the gray background shows the entire alloy design space, and the red (darker in b/w print) regions show the alloys with various contents of Re, Cr, or Al. The values for the well-known commercial superalloys are also provided.[51–53] When investigating the scatter plots in Figures 6(d) through (l), note that the histograms in Figures 6(a) through (c) show the population density of the M_d values in the scatter plots. Hence, one can see, for example, the M_d values are not equally distributed in a red

Fig. 6—Percentage of alloys in given M_d ranges shown in (*a*) through (*c*). ▶ Scatter plots display M_d *vs* the volume fraction of the γ' for different concentrations of Re (*d* through *f*), Cr (*g* through *i*), and Al (*j* through *l*). The triangle, circle, and diamond show the first (CMSX-2)-,[51] second (CMSX-4)-,[52] and third (CMSX-10)-generation[53] superalloys, respectively.

region. Although very weak, a shift toward a lower volume fraction of γ' and a higher M_d number is observed in alloys with a higher Re content (Figures 6(e), (f), and (g)). A higher alloy density and a lower volume fraction of γ' with increased Re are also predicted by the ANN model. These predictions corroborate with the literature, and that is why recent activities have focused on developing high creep-resistant alloys with low levels of Re.[49]

Cr, a γ-forming and fast diffusing element in the matrix,[2] clearly decreases the rupture life as seen in Figure 5. Similar to Re, Cr has a high propensity to form the brittle TCP phases, which reduce the creep resistance of an alloy. The presence of Cr in an alloy increases the partitioning of the refractory elements to the matrix,[54] and so enhances the formation of the TCP phases. This claim is supported by M_d *vs* the volume fraction of the γ' scatter plots for the alloys with various Cr contents as seen in Figures 6(g), (h), and (i). Increasing amount of Cr shifts the alloy design space toward the region with lower volume fraction of γ' and higher values of M_d. The observed shift is more discerned with Cr than Re. While the presence of Cr is necessary for the hot corrosion and oxidation resistance, a low Cr content is beneficial for the rupture strength and stability of the microstructure. Hence, in later generation superalloys, the Cr level is reduced to less than 4 wt pct to accommodate more useful refractory elements.[54,55]

Al is an essential element for oxidation resistance due to formation of the Al_2O_3 oxide layer. Moreover, it is the major element in the strengthening γ' phase and is a solid solution strengthener in the matrix, yet Figure 5

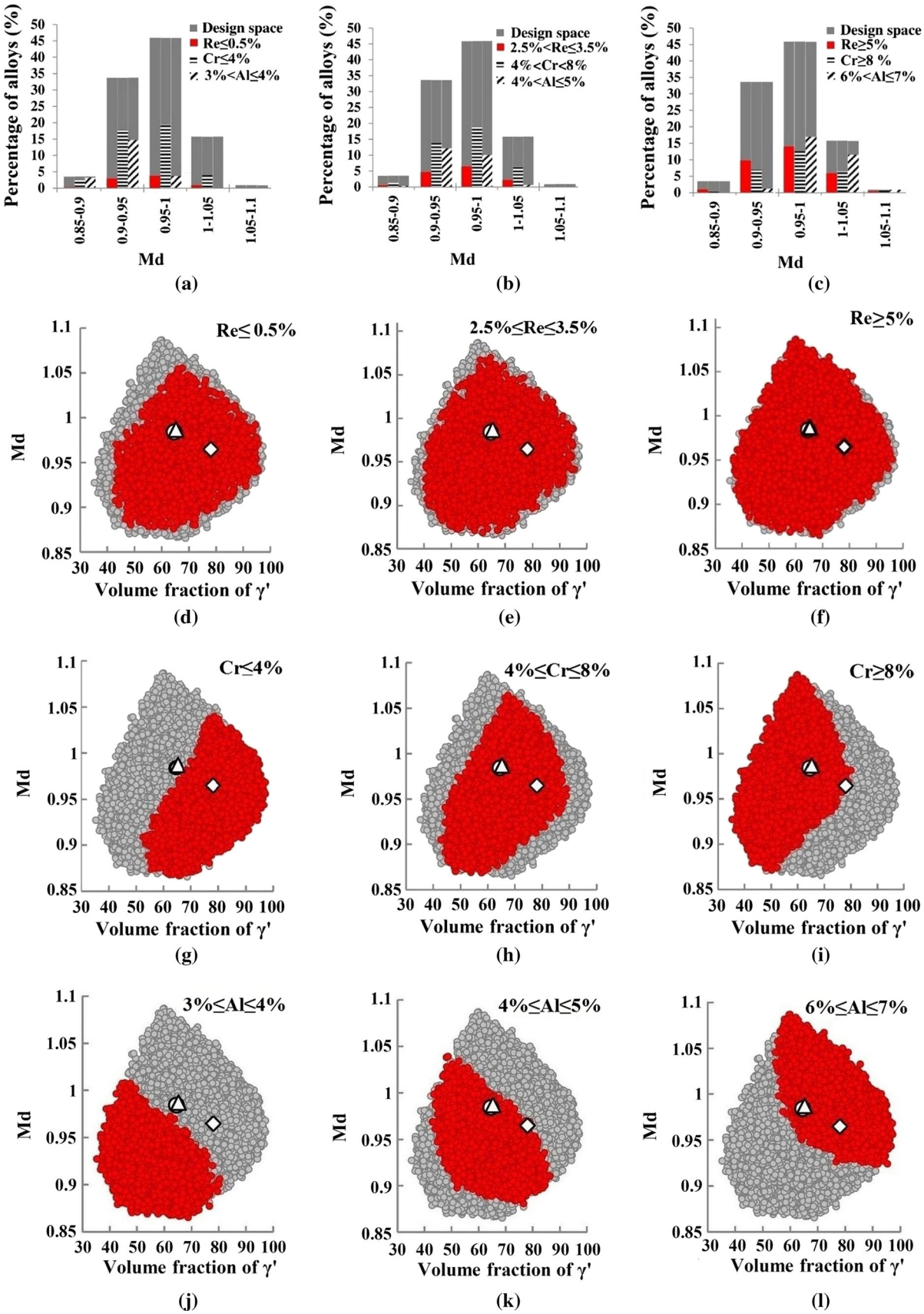
Percentage of alloys (%)
Design space
Re≤0.5%
Cr≤4%
3%<Al≤4%
0.85-0.9
0.9-0.95
0.95-1
1-1.05
1.05-1.1
Md
(a)
Design space
2.5%<Re≤3.5%
4%<Cr<8%
4%<Al≤5%
(b)
Design space
Re≥5%
Cr≥8 %
6%<Al≤7%
(c)
Re≤ 0.5%
2.5%≤Re≤3.5%
Re≥5%
Volume fraction of γ'
(d)
(e)
(f)
Cr≤4%
4%≤Cr≤8%
Cr≥8%
(g)
(h)
(i)
3%≤Al≤4%
4%≤Al≤5%
6%≤Al≤7%
(j)
(k)
(l)

suggests that its content should be adjusted carefully for an increased rupture life. Figures 6(j), (k), and (l) show the plots of M_d *vs* the volume fraction of γ' for various Al concentrations. As shown before, M_d *vs* the volume fraction of γ' shows an inverse relationship for Re and Cr. In contrast, alloys with higher Al content have higher volume fraction of γ' and higher M_d values. Moreover, the plots show a very discernible increase in the M_d value with a slight increase in the Al content. Although Al is the main γ' forming element, its excessive usage diminishes the high temperature stability of the alloys by making them prone to precipitation of the TCP phases.[56] Therefore, increasing the Al content increases both the volume fraction of γ' and the M_d values.

Two other major elements used in superalloys are the refractory W and Ta, and the ratio of Ta/W is important in the alloy design. From the processing point of view, a high Ta/W ratio is reported to increase the interface stability and reduce the extent of the freckling type casting defects caused by convective instabilities during solidification processing.[57] Ta, by segregating into the interdendritic regions, alleviates density inversion in these regions induced by the W segregation to the dendritic cores. Thus, a Ta/W ratio around unity is beneficial. Hence, the Ta/W ratio can give a hint on the manufacturability of alloys as single crystals. In addition, it has been reported that alloys with the ratios close to the unity have the best hot corrosion resistance.[58] The ANN modeling results of the current study predicts these reported experimental findings. The rupture strength in Figure 5 increases until this ratio becomes unity and then it decreases. The effect of this ratio on the creep properties relies also on the Ta/W relation to the γ' phase fraction. At a given Al concentration, Ta increases the volume fraction of γ', while alloying elements like W, Mo, Cr, and Re decrease it.[2] It has been also shown that the variation of the Ta/W ratio has a significant effect on the size and morphology of the γ' phase in single-crystal superalloys, both of which are a strong function of the test temperature and misfit that determine the creep strength of the alloys.[58] Increasing this ratio may lead to changing the shape from the cuboidal to the spheroidal one which reduces the rupture life.

The rupture life of the designed alloys can be screened for selected elements and parameters. An example is shown for Re, considering the density, volume fraction of γ', and the M_d values in a series of scatter plots presented in Figure 7. The gray background shows the entire alloy design space, and the red (darker in b/w print) regions show the alloys with Re content similar to those in the 1st, 2nd, and 3rd generation single-crystal superalloys in the respective columns. The first row (Figures 7(a) through (c)) shows distribution of alloys with respect to the rupture time for varying Re contents. While interpreting these histograms, the population density distribution of the red (rupture time) is a more important parameter than the ratio of the total red to the total gray bars. Figures 7(d) through (f) show an overall sigmoid relationship between the rupture life and the alloy density with a large variation in both the axes. The overall trend of the data indicates about 1000-hour increase in the creep life for a 1 g/cm^3 density rise. However, the creep life exists in a broad band for a given density. Closeness of the experimental data [51–53] (filled symbols) presented in the design space to the artificial neural network predictions (empty symbols) for well-known first (CMSX-2: triangle)-, second (CMSX-4: circle)-, and third (CMSX-10: diamond)-generation commercial superalloys displays the prediction accuracy of the artificial neural network. The rupture life increases with addition of Re (Figures 7(a) through (f), red regions). A striking observation is, however, that alloys with a high amount of Re (Figures 7(c) and (f)) are not necessarily the best creep-resistant ones and the rupture life spans a large range from about 100 to 1000 hours. This shows the unavoidable effect of the other elements than Re and the current artificial neural network demonstrates this nicely.

Figures 7(g) through (i) show that in the entire design space, alloys with the γ' volume fractions around 55 to 65 pct have the highest rupture strengths, which is in accord with the data published for some advanced single-crystal nickel-based superalloys.[1,2,15] The rupture strength decreases when moving away from these values. For high rupture strength alloys, the range within which the γ' volume fraction varies gets narrower. It is noteworthy that dependency of the rupture life on the γ' volume fraction is high and positive on the low-fraction boundary (left), while it is lower and negative on the high-fraction boundary (right). The dependency may be seen by the slopes of the lines that may be drawn on the left and right boundaries of the scatter plots in Figures 7(g) through (i). The role of the Re addition on the rupture life is prevalent in Figures 7(g) through (i), but that on the γ' volume fraction is vague. Figures 7(j) through (l) indicate an M_d value of about 0.98 to yield the highest creep lives in the design space. Again, the role of the Re addition on M_d is not obvious in these figures. The reduced γ' volume fraction and increased M_d with the Re additions are seen, however, in Figures 6(a) through (c).

The combined effect of elements is shown for two groups of alloys in Figures 7(f), (i), and (l). As described earlier, the red region, whose boundary is outlined with dots, shows alloys containing Re greater than 5 wt pct. The first overlaid group contains Re and Cr and is shown by the color green, whose boundary is outlined with a white line. The second group contains Re, Cr, Ta, and Al and is shown by the color light blue, whose boundary is outlined with a dashed line. The element contents in both the groups are equivalent to those in the 3rd generation superalloys. It is clearly illustrated by these figures that the artificial neural network results can be post-processed to highlight any alloy composition ranges for any investigated property. In fact, investigated properties for definite alloy compositions are already shown for well-known commercial superalloys as illustrated in Figures 6 and 7. Data for ERBALLOY (□) are also shown in Figures 7 (f), (i), and (l). ERBALLOY has a rupture time slightly greater than the CMSX-4, and its composition differs from that of the CMSX-4 only by 2 wt pct more Re.

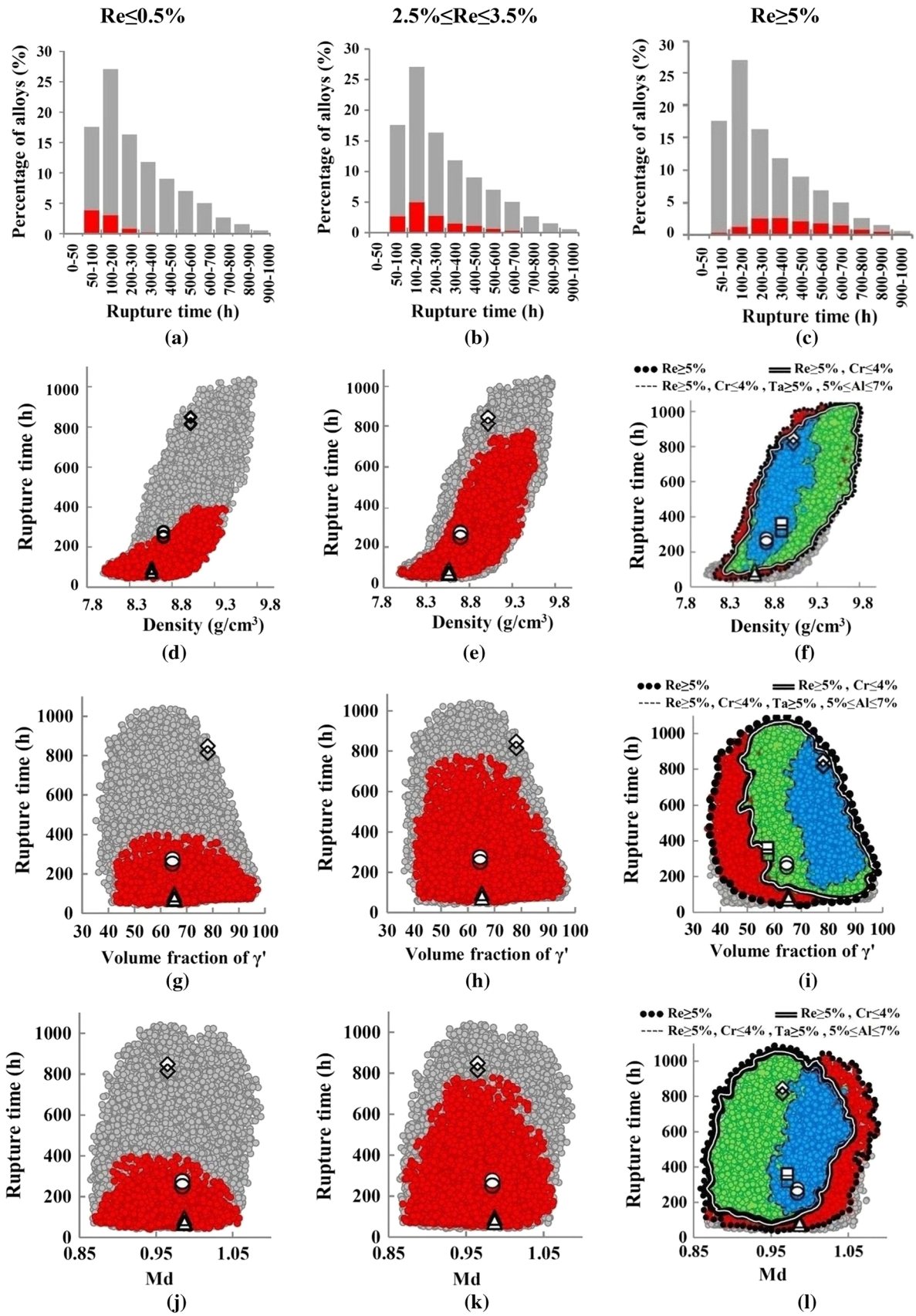

Fig. 7—Percentage of alloys in given rupture time ranges shown in (*a*) through (*c*). Rupture time *vs* density (*d* through *f*), volume fraction of γ' (*g* through *i*), and M_d (*j* through *l*) are plotted. The data for the experimental alloy (ERBALLOY) of this study are also shown as square symbols. See the text for other symbols.

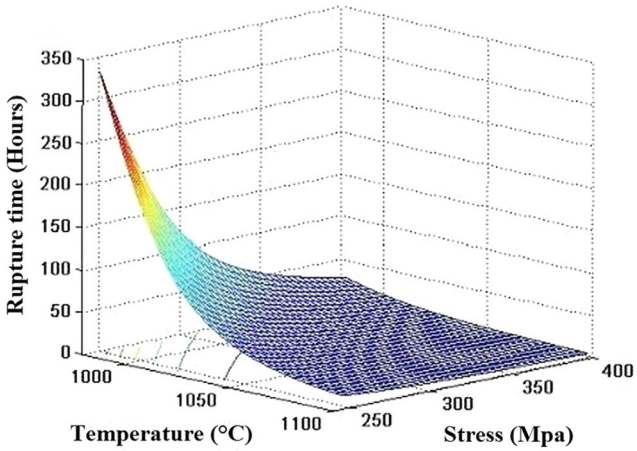

(a)

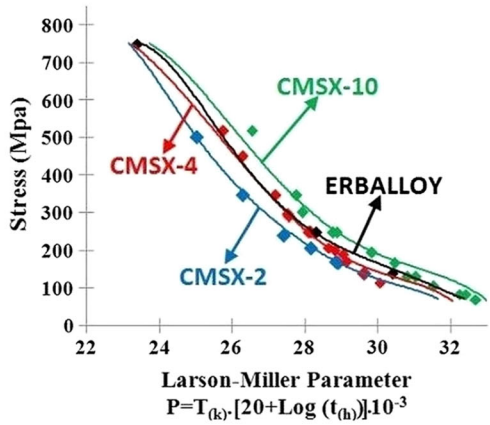

(b)

Fig. 8—Temperature–stress–rupture time plot (*a*) for ERBALLOY and Larson–Miller plots (*b*) for selected alloys. Continuous lines in (b) show the ANN modeling results, whereas the dotted lines show the experimental values.

Figure 8(a) shows the artificial neural network-predicted influence of temperature and stress on the rupture time of ERBALLOY. It is observed that with increasing temperature, time to rupture decreases at all stress values. The rate of decrease, however, is lower at higher stresses. The same is true for the effect of the stress and the results show that at higher temperatures, the dependency of the rupture strength to the stress decreases. Interactions between the temperature, stress, and rupture time are better presented by the Larson–Miller plots.[2] Figure 8(b) shows the artificial neural network-modeled Larson–Miller plots (continuous lines) for the first (CMSX-2)-, second (CMSX-4)-, and third (CMSX-10)-generation alloys as well as for ERBALLOY. Experimental data points are also shown for the commercial alloys from the literature[51–53] and for ERBALLOY. A close agreement is evident between the experimental and artificial neural network-predicted Larson–Miller plots.

Influence of the major elements on the density is shown in Figure 9 for ERBALLOY. The effect of each alloying element on the density is studied by varying the concentration of that element only, compensated by the Ni content while keeping the content of the other elements fixed. This plot is generated to show the capabilities of the artificial neural network model for the density estimation, and similar plots can obviously be generated for any alloy composition. The plot simply shows variation in the density, which is related to the amount of the elements in the alloy and their atomic weights. The data point symbol corresponding to an element's concentration in ERBALLOY is made larger in Figure 9. A careful look will discern that the larger symbols are all at correct density value of 8.88 g/cm^3 for ERBALLOY, which again indicates the prediction capability of the ANN model. It is apparent that elements with atomic weights larger than Ni increase the density of the alloy and vice versa. Co has almost a neutral effect on the density. The refractory elements like Re and W, which increase the creep resistivity of the alloy, increase the density of the alloy and therefore their addition should be done with caution to have a balance between the density and creep resistivity.

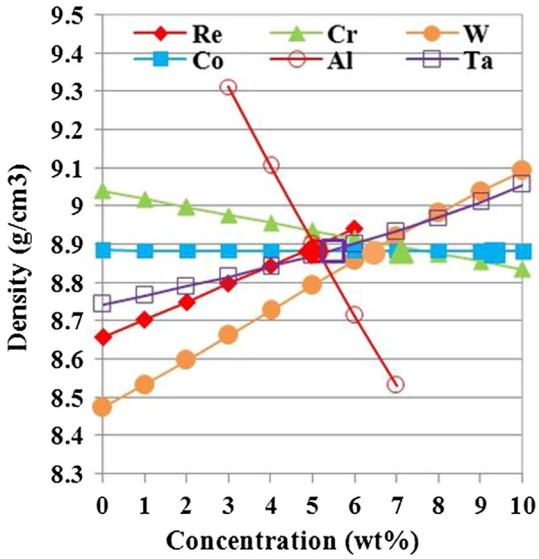

Fig. 9—Density variation of ERBALLOY with concentration of the elements.

The results of this integrated artificial neural network alloy design study can be used to suggest alloys with superior properties compared to existing commercial superalloys. Figure 7 can be utilized for such purpose as it shows rupture time for all 45,000 alloys in the design space and for selected commercial alloys. Although hundreds of alloys with superior properties can be screened out, Table III lists ten alloys in each of the first-, second-, and third-generation single-crystal superalloy groups. A well-known commercial alloy precedes the list in each group. The listed alloys are selected with a lower density and a greater rupture time than the commercial alloy in each generation. As already discussed before, while moving from the first-generation to

Table III. Suggested First-, Second-, and Third-Generation Superalloys

Alloy	Cr	Co	Re	W	Al	Ta	Ti	Mo	Hf	Density (g/cm^3)	γ' Vol. (Pct)	M_d eV	Ta/W	Rupture Time (h)
First-Generation Single-Crystal Superalloys														
CMSX-2	8	4.6	—	7.9	5.6	5.8	0.9	0.6	—	8.56	64	0.987	0.73	74
1	9.19	8.75	0.15	5.35	6.51	5.06	1	0.6	0.1	8.29	67	0.993	0.95	74
2	9.95	5.21	0.44	6.91	6.10	5.40	1	0.6	0.1	8.43	63	0.998	0.78	74
3	7.9	6.3	—	7.6	6.2	5.7	1	0.6	0.1	8.47	68	0.993	0.75	77
4	9.23	6.82	0.39	6.41	6.03	6.49	1	0.6	0.1	8.48	64	0.997	1.01	80
5	9.6	4.9	0.2	6.4	5.6	6.7	1	0.6	0.1	8.55	62	0.989	1.03	85
6	10	2	0.36	6.62	5.56	6.85	1	0.6	0.1	8.56	62	0.992	1.04	96
7	8.9	3.9	0.3	6.6	5.7	6	1	0.6	0.1	8.52	65	0.984	0.92	98
8	9.06	2	—	7.39	5.84	6.81	1	0.6	0.1	8.55	66	0.995	0.92	105
9	8.2	6.5	0.1	5.4	5.2	4.1	1	0.6	0.1	8.50	65	0.953	0.75	135
10	8.4	8.3	0.2	4.5	5.3	4.4	1	0.6	0.1	8.46	64	0.955	0.97	146
Second-Generation Single-Crystal Superalloys														
CMSX-4	6.5	9	3	6	5.6	6.5	1	0.6	0.1	8.7	65	0.985	1.08	275
1	5.84	7.10	3.03	9.96	6.60	6.98	1	0.6	0.1	8.68	68	1.001	0.70	277
2	6.79	8.50	3.19	8.26	6.33	7.94	1	0.6	0.1	8.66	66	1.000	0.96	279
3	6.79	6.08	2.75	7.89	5.91	6.55	1	0.6	0.1	8.69	69	0.996	0.83	287
4	5.09	7.75	2.5	8.36	6.30	7.01	1	0.6	0.1	8.70	67	1.003	0.84	291
5	4.33	8.85	2.5	7.71	6.06	7.08	1	0.6	0.1	8.69	65	0.997	0.92	292
6	4.92	9.83	3.5	6.98	6.44	7.05	1	0.6	0.1	8.67	66	0.992	1.01	303
7	7.07	2.74	3.5	7.11	6.50	8.69	1	0.6	0.1	8.68	70	0.992	1.22	307
8	6.15	2.72	3.5	7.15	6.00	6.68	1	0.6	0.1	8.67	69	0.997	0.94	326
9	6.29	6.45	2.54	8.93	6.29	8.00	1	0.6	0.1	8.70	70	0.996	0.90	346
10	6.65	3.15	2.69	9.13	6.42	8.26	1	0.6	0.1	8.70	69	0.999	0.90	362
Third-Generation Single-Crystal Superalloys														
CMSX-10	2	3	6	5	5.7	8	0.2	0.4	—	9.05	77	0.965	1.60	840
ERBALLOY	7.1	9.3	5	6.5	5	5.5	1	0.6	0.1	8.88	58	0.971	0.85	361
1	0.86	3.88	5	8.54	6.19	10	1	0.6	0.1	9.02	78	1.015	1.17	841
2	0.94	7.37	6	10	6.42	8.13	1	0.6	0.1	9.03	75	1.022	0.81	842
3	0.45	10	5.29	9.81	6.43	7.96	1	0.6	0.1	9.01	76	1.015	0.81	842
4	0.32	6	5.09	8.16	6.24	9.84	1	0.6	0.1	9.04	75	1.012	1.21	843
5	2.42	0.51	5.13	10	5.96	8.24	1	0.6	0.1	9.03	74	1.010	0.82	843
6	1.69	6.80	6	8.04	5.92	8.11	1	0.6	0.1	9.02	73	1.002	1.01	844
7	1.51	5.22	5.69	10	6.42	6.98	1	0.6	0.1	8.98	76	1.014	0.70	855
8	0.76	9.02	5.25	9.58	6.02	8.23	1	0.6	0.1	9.05	74	1.007	0.86	875
9	0.50	7.32	5.13	10	6.54	8.38	1	0.6	0.1	9.00	76	1.023	0.84	894
10	0.30	8.01	5.74	9.14	6.30	8.62	1	0.6	0.1	9.05	76	1.013	0.94	895

Element contents are in wt pct.

the third, the Cr content decreases, the Re content increases, and the gamma-prime precipitate volume fraction increases. The Al content is selected to be 5 to 6 pct which is, in general, the amount in commercial superalloys. The Ta/W ratio and M_d values are around unity, which provides the highest rupture time.

The foregoing has presented that the ANN alloy design is a powerful method with highly accurate prediction of the alloy properties. The ANN method can use results from the PHACOMP and CALPHAD-based methods as inputs. Alternatively, the results of the three methods can be utilized in the post-processing step to establish correlations between the microstructure, property, and performance. In addition, the ANN results can be transferred to a CALPHAD-based modeling platform to predict solidification and heat-treated microstructures. Conversely, composition modeling can, of course, be done by using only the PHACOMP or CALPHAD-based methods. However, this requires a sequential treatment of several microstructural entities, thermodynamic properties, mechanical properties, and employment of a multitude numbers of phase diagrams. Nevertheless, this is very cumbersome, and trustable simulation correlations between the composition of a multicomponent alloy and its mechanical properties are still in their infancy.[8–12] Evidently, an integrated ANN modeling can provide a faster route to finding a correct composition window and establishing a sound composition–microstructure–property relationship. Obviously, ANN modeling requires an access to a reliable alloy property database, which itself is not easily available and a tedious work to compile.

IV. CONCLUSIONS

Designing superalloys with increased temperature capability, improved life, and reduced density is of a crucial importance in aerospace and power industries. A

multilayer perceptron (MLP) feed-forward (FF) artificial neural network (ANN) with Bayesian regularization (BR) backpropagation algorithm is developed and used to model the density and rupture time of single-crystal superalloys. The input to the network are the composition for the density modeling and the composition, density, precipitate volume fraction, temperature, and stress for the creep life modeling. The precipitate volume fraction is calculated *via* the PHACOMP method. Propensity for the TCP phase formation is also determined by the PHACOMP method and is used in post-processing of the ANN results. The results are presented in scatter plots, which show effect of Re, Cr, Al, and the Ta/W ratio on the density, creep life, precipitate volume fraction, and TCP propensity. In addition, Larson–Miller plots are generated for known commercial alloy compositions. The ANN model validation is carried out by comparing the ANN predictions with the experimental literature data and with the data produced in the present study for an experimental alloy of a 3rd generation composition. The predictions are in close agreement with the experimental data. Before determining the creep lives for the experimental alloy, the solidification behavior of the alloy is studied by a CALPHAD-based software, and then single-crystal rods are grown by the Vertical Bridgman method for preparing creep test samples. It is shown that ANN model unveils the complex correlations between the microstructure, application parameters, and the properties, so it is a powerful alloy design approach with highly accurate predictions of the alloy properties. Furthermore, the ANN results can be transferred to thermodynamics-based modeling platforms to predict alloy solidification and heat-treated microstructures. Thus, the ANN modeling can facilitate in finding the correct composition window and final microstructure/properties of the product, which can help reduce the material development cycle time.

ACKNOWLEDGMENT

This work was supported by the Scientific and Technological Research Council of Turkey, TUBITAK, under grant number 112M783.

REFERENCES

1. T.M. Pollock, S. Tin, and J. Propuls: *Power*, 2006, vol. 22 (2), pp. 361–74.
2. R.C. Reed: *Superalloys, Fundamentals and Applications*, Cambridge University Press, Cambridge, 2006, pp. 122–30.
3. A. Sato, J.J. Moverare, M. Hasselqvist, and R.C. Reed: *Metall. Mater. Trans. A*, 2012, vol. 43 (7), pp. 2302–15.
4. S. Drawin and J. Justin: *AerospaceLab,* 2011, no. 3, pp. 1–13.
5. R.E. Schafrik and S. Walston: *Superalloys 2008*, TMS, Warrendale, PA, 2008, pp. 3–9.
6. N.R. Council: *Integrated Computational Materials Engineering*, National Academies Press, Washington, DC, 2008.
7. J.H. Panchal, S.R. Kalidindi, and D.L. Mc Dowell: *Comput. Des.*, 2013, vol. 45 (1), pp. 4–25.
8. J.O. Andersson, T. Helander, L. Hdghmd, P. Shi, and B. Sundman: *Pergamon Calphad*, 2002, vol. 26 (2), pp. 273–312.
9. W. Cao, S.-L. Chen, F. Zhang, K. Wu, Y. Yang, Y.A. Chang, R. Schmid-Fetzer, and W.A. Oates: *Calphad*, 2009, vol. 33 (2), pp. 328–42.
10. Z. Guo, N. Saunders, A.P. Miodownik, and J.-P. Schillé: *Mater. Sci. Eng. A*, 2005, vols. 413–414, pp. 465–69.
11. R.C. Reed, T. Tao, and N. Warnken: *Acta Mater.*, 2009, vol. 57, pp. 5898–5913.
12. D.J. Crudden, B. Raeisinia, N. Warnken, and R.C. Reed: *Metall. Mater. Trans. A*, 2013, vol. 44 (5), pp. 2418–30.
13. P. Caron: *Superalloys 2000*, TMS, Warrendale, PA, 2000, pp. 737–64.
14. R.A. MacKay, T.P. Gabb, J.L. Smialek, and M.V. Nathal: *JOM*, 2010, vol. 62 (1), pp. 48–54.
15. E. Fleischmann, M.K. Miller, E. Affeldt, and U. Glatzel: *Acta Mater.*, 2015, vol. 87, pp. 350–56.
16. Y. Murata, S. Miyazaki, M. Morinaga, and R. Hashizume: *Superalloys 1996*, TMS, Warrendale, PA, 1996, pp. 61–70.
17. N. Yukawa, M. Morinaga, Y. Murata, H. Ezaki, and S. Inoue: *Superalloys 1988*, TMS, Warrendale, PA, 1988, pp. 225–34.
18. K. Matsugi, Y. Murata, M. Morinaga, and N. Yukawa: *Superalloys 1992*, TMS, Warrendale, PA, 1992, pp. 307–16.
19. N.S. Reddy, J. Krishnaiah, S.G. Hong, and J.S. Lee: *Mater. Sci. Eng. A*, 2009, vol. 508, pp. 93–105.
20. W. You, Y.X. Liu, B.Z. Bai, and H.S. Fang: *J. Iron Steel Res. Int.*, 2008, vol. 15 (2), pp. 87–90.
21. Z. Sterjovski, D. Nolan, K.R. Carpenter, D.P. Dunne, and J. Norrish: *J. Mater. Process. Technol.*, 2005, vol. 170 (3), pp. 536–44.
22. S. Rath, P. Talukdar, and A.P. Singh: *Am. J. Neural Netw. Appl.*, 2017, vol. 3 (3), pp. 36–39.
23. Z. Guo and W. Sha: *Comput. Mater. Sci.*, 2004, vol. 29, pp. 12–28.
24. S. Mandal, P.V. Sivaprasad, S. Venugopal, K.P.N. Murthy, and B. Raj: *Mater. Sci. Eng. A*, 2008, vol. 485 (1–2), pp. 571–80.
25. S. Malinov and W. Sha: *Mater. Sci. Eng. A*, 2004, vol. 365 (1–2), pp. 202–211.
26. S. Al-Lubani: *Int. J. Mech. Prod. Eng. (IJMPE)*, 2018, vol. 6 (5), pp. 15–18.
27. R.S. Yassar, O. AbuOmar, E. Hansen, and M.F. Horstemeyer: *Mater. Des.*, 2010, vol. 31, pp. 3683–89.
28. B.D. Conduit, N.G. Jones, H.J. Stone, and G.J. Conduit: *Scripta Mater.*, 2018, vol. 146, pp. 82–86.
29. J. Warde and D.M. Knowles: *ISIJ Int.*, 1999, vol. 39 (10), pp. 1015–19.
30. F. Tancret and H.K.D.H. Bhadeshia: *Mater. Sci. Technol.*, 2003, vol. 19, pp. 283–90.
31. S.B. Singh, H.K.D.H. Bhadeshia, D.J.C. MacKay, H. Carey, and I. Martin: *J. Ironmak. Steelmak.*, 1998, vol. 25 (5), pp. 355–65.
32. I. Grešovnik, T. Kodelja, R. Vertnik, and B. Šarler: *Proc. 15th IASTED, Int. Conf. Artif. Intell. Soft Comput.*, Acta Press, Napoli, Italy, 2012, pp. 249–255.
33. L.A. Dobrzański, M. Gawron, and M. Berliński: *Arch. Mater. Sci. Eng.*, 2014, vol. 67 (1), pp. 32–38.
34. S.K. Singha and S.J. Singh: *Int. J. Res. Eng. Technol.*, 2015, vol. 4 (1), pp. 24–29.
35. L.A. Dobrzański, M. Sroka, and J. Dobrzański: *J. Achiev. Mater. Manuf. Eng.*, 2007, vol. 20 (1–2), pp. 303–06.
36. N. Bano and M. Nganbe: *J. Mater. Eng. Perform.*, 2013, vol. 22 (4), pp. 952–57.
37. J. Jones and D.J.C. MacKay: *Superalloys 1996*, TMS, Warrendale, PA, 1996, pp. 417–24.
38. I. Di Martino, J.W. Brooks, P.A.S. Reed, P. Holdway, and A. Wisbey: *Mater. Sci. Technol.*, 2007, vol. 23 (12), pp. 1402–07.
39. B.D. Conduit, N.G. Jones, H.J. Stone, and G.J. Conduit: *Mater. Des.*, 2017, vol. 131, pp. 358–65.
40. D.J. Crudden, B. Raeisinia, N. Warnken, and R.C. Reed: *Metall. Mater. Trans. A*, 2013, vol. 44A, pp. 2418–30.
41. S. Yoshitake, V. Narayan, H. Harada, H.K.D.H. Bhadeshia, and D.J.C. Mackay: *ISIJ Int.*, 2008, vol. 38 (5), pp. 495–502.
42. G. Zhang, B.E. Patuwo, and M.Y. Hu: *Int. J. Forecast.*, 1998, vol. 14, pp. 35–62.
43. K. Hornik, M. Stinchcombe, and H. White: *Neural Netw.*, 1990, vol. 3 (5), pp. 551–60.

44. D.J.C. MacKay: *Bayesian Methods for Backpropagation Network. Models of Neural Networks III*, Springer, New York, 1996, pp. 211–54.
45. D.M. Titterington: *Stat. Sci.*, 2004, vol. 19 (1), pp. 128–39.
46. M. Montakhab and E. Balikci: *Metall. Mater. Trans. A*, 2016, vol. 47A, pp. 3031–39.
47. W. Qiong, L. Shu-Suo, M. Yue, and G. Sheng-Kai: *Chin. Phys. B*, 2012, vol. 21 (10), p. 109102.
48. C.L. Fu, R. Reed, A. Janotti, and M. Krcmar: *Superalloys 2004*, TMS, Warrendale, PA, 2004, pp. 867–76.
49. M. Huang and J. Zhu: *Rare Met.*, 2016, vol. 35 (2), pp. 127–39.
50. R. Darolia, D.F. Lahrman, R.D. Field, and R. Sisson: *Superalloys 1988*, TMS, Warrendale, PA, 1988, pp. 255–64.
51. K. Harris and G. L. Erickson: Cannon-Muskegon Corporation, *U.S. patent 4582548*, CMSX-2 Alloy, 1986.
52. K. Harris, G.L. Erickson, W.D. Brentnall, J.M. Aurrecoechea, S.L. Sikkenga, and K.G. Kubarych: *Superalloys 1992*, TMS, Warrendale, PA, 1992, pp. 297–306.
53. G.L. Erickson: *Superalloys 1996*, TMS, Warrendale, PA, 1996, pp. 35–44.
54. Z. Shi, S. Liu, X. Wang, and J. Li: *trans. Nonferrous Met. Soc. China*, 2015, vol. 25 (3), pp. 776–82.
55. M. Moniruzzaman, Y. Murata, M. Morinaga, N. Aoki, T. Hayashida, and R. Hashizume: *ISIJ Int.*, 2002, vol. 42 (9), pp. 1018–25.
56. P. Caron and T. Khan: *Aerosp. Sci. Technol.*, 1999, vol. 3 (8), pp. 513–23.
57. C. Beckermann, J.P. Gu, and W.J. Boettinger: *Metall. Mater. Trans. A*, 2000, vol. 31A, pp. 2545–57.
58. T. Yamagata, H. Harada, S. Nakazawa, and M. Yamazaki: *Trans. Iron Steel Inst. Jpn.*, 1986, vol. 26 (7), pp. 638–41.